Journal of Engineering and Technology for Industrial Applications

ITEGAM-JETIA

Manaus, v.11n.55, p. 29-47. September/October, 2025.
DOI: https://doi.org/10.5935/jetia.v11i55.1854

ISSN ONLINE: 2447-0228

RESEARCH ARTICLE OPEN ACCESS

ASSESSMENT OF SOLAR CHIMNEY POWER PLANT PERFORMANCE UNDER VARIOUS PARAMETERS

Farid Gaci[1], Mohamed Walid Azizi[2], Ahcene Akni[3], Moumtez Bensouici[4], Djoubeir Debbah[5]

[1, 3] Department of Transportation Engineering, Frères Mentouri University -Constantine 1, Algeria.
[2, 4, 5] Department of Mechanical Engineering and Electromechanical, Abdelhafid Boussouf University- Mila, Algeria.

[1] https://orcid.org/0009-0000-9487-4929, [2] http://orcid.org/ 0000-0003-1066-740X
[3] https://orcid.org/0000-0002-3180-4218, [4] http://orcid.org/ 0000-0002-5855-1775
[5] http://orcid.org 0009-0003-8797-2952

Email: farid.gaci@umc.edu.dz, medwalid.azizi@centre-univ-mila.dz, akni.ahcene@umc.edu.dz, moumtez.bensouici@umc.edu.dz, debbah.dj@centre-univ-mila.dz

ARTICLE INFO

Article History
Received: April 12, 2025
Revised: May 20, 2025
Accepted: September 15, 2025
Published: September 30, 2025

Keywords:
Solar chimney,
Turbulence model,
Natural convection,
Power,
Radiation.

ABSTRACT

This numerical study primarily seeks to illustrate that the power output of a solar chimney is determined by the equilibrium between a geometry designed to enhance thermal draft and a turbulence model that faithfully captures the physics of the flow. Several turbulence models were used to evaluate their ability to simulate flows and heat transfer within the solar chimney. A Discrete Ordinates approach was adopted to solve the radiative transfer equation and to refine performance predictions and guide the optimization of geometric and thermal parameters. The most appropriate RNG k-ε turbulence model highlighted notable differences in the distribution of dynamic and thermal fields compared to other turbulence models used. For example, the maximum variation compared to the standard k-ε model reached 0.47 m/s for velocity, 6.55 m²/s² for temperature and 15.07 K for turbulent kinetic energy. Additionally, the study highlighted the critical impact of geometric parameters on solar chimney performance. Increasing the height of the solar chimney by 25% to 50%, for example, could boost power output by 26 % to 52 %. These results highlight key areas for improvement, paving the way for a more efficient design of this type of energy system.

I. INTRODUCTION

Renewable energies play a key role in the fight against climate change, offering a clean and sustainable alternative to conventional energy sources. Among these technologies, the solar chimney stands out as an innovative solution for electricity production. It works by capturing the sun's thermal energy to generate an upward airflow, which drives a turbine connected to an electrical generator. Experimental scientific studies have been conducted in this context. These are often accompanied by other, less expensive, complementary approaches based on numerical simulation, which allow the modeling of airflows and heat transfers in solar chimney power plants (SCPPs) with the aim of reducing electricity production costs and thus enhancing the efficiency and viability of this technology for large-scale applications, particularly in sunny regions.

Research on solar chimneys has been developed through various studies, ranging from experimentation with small prototypes to more sophisticated approaches, integrating numerical simulations to improve the design and performance of solar chimney power plants.

Schlaich's investigations [1] focused on the first solar chimney prototype built in Manzanares in 1982. Since then, much work has been done by scientists and researchers on the Solar Chimney Power Plant (SCPP). In their experimental study, N. Pasumarthi and S. A. Sherif [2] examine a solar chimney, making two improvements to the collector aimed at enhancing the temperature and air flow to maximize the power output. Das P and Chandramohan VP [3], [4] have developed a compact Solar Chimney Power Plant in India, which includes a chimney measuring 6 meters in height, with a radius of 0.3 m and an inclination of 30 degrees, as well as a radius of

1.75 m. Additionally, a parametric study was performed where the diverging angles were adjusted between 1° and 5 °. The findings revealed that the chimney achieved its best performance at a diverging angle of 2 °.

Ahmed et al. [5] conducted a review of hybrid solar chimney systems integrated with photovoltaic panels, solar ponds, or geothermal energy, assessing their efficiency gains and suggesting avenues for enhancement. A double-pass canopy was designed by Nasraoui et al. [6], resulting in a 28% improvement in collector efficiency. Murena et al [7] evaluated the performance of a pilot solar chimney, tested over a period of seven months in southern Italy, providing new insights, particularly on the impact of ambient humidity. Kumar,et al. [8] conducted a review that analyzes the heat demand across various sectors, addresses the challenges of integrating solar energy (such as sunlight availability, costs, and compatibility), and suggests strategies to enhance this energy transition. Ayadi et al. [9] studied by simulation adopting the k-ε turbulence model four turbine diameters to analyze their impact on the local airflow characteristics in the SCPP, using ANSYS Fluent 17. In addition, they highlighted the significant impact of the collector roof height on the performance of the SCPP. In their study, [10] quantitatively evaluated the effect of various types of collectors on the performance of chimney solar power plants.

The integration of a second roof in the collector section helps to increase the temperature as well as the airflow velocity, which improves the efficiency of the system. Fallah and Valipour [11] conducted a study that demonstrated that artificial roughness applied to the bottom surface of the collector increases heat transfer to the air while decreasing the airflow velocity. The system exhibited superior performance when the roughness was concentrated around the collector opening. Kebabsa et al. [12] investigated the impact of collector entry shape on the performance of solar chimney power plants. Their research revealed that a solar chimney featuring a collector distance of 0.8 meters and a slope of 9.1 degrees produces 16 % more electricity compared to a flat collector design. Guo et al. [13] used a three-dimensional numerical approach incorporating radiation models, demonstrating that this model is essential to avoid overestimating the absorbed energy. Furthermore, the ambient temperature mainly influences the air velocity without significantly affecting the energy production of the SCPP. Mebarki et al. [14] employed computational fluid dynamics to investigate how the geometric scale factor influences the implementation of the SUT in urban environments. Hassan et al. [15] conducted a parametric three-dimensional computational fluid dynamics (CFD) analysis to investigate how the angles of the collector slope and chimney divergence affect the performance of the Manzanares prototype. The numerical simulations, which were validated against experimental data, employed the RNG k-ε turbulence model.

Maia et al. [16] performed a numerical analysis of the turbulent flow inside a solar chimney by adopting the standard k-ε model. An elaborate model was implemented to examine the impact of the main geometric parameters on airflow behavior. Mohamad et al. [17] conducted a study using 2D numerical analysis to assess the performance of a solar tower power plant by varying geometric and environmental parameters. The findings indicate that a negatively inclined collector and an increased divergent angle enhance both air velocity and power output. Awan et al. [18] conducted a study that aims to design, optimize and evaluate the performance of a solar chimney power plant, with optimization of design parameters such as tower height and thermal storage. Torabi et al. [19] examined how geometric parameters and boundary conditions influence the performance of the SUT, finding that both the angle of the chimney divergence and the rate of radiation significantly affect power generation.

Furthermore, it is noted that many studies in computational fluid dynamics (CFD) have favored a single turbulence model without exploring other alternatives. Thus, the research of Siyang M. Jirena et al. [20] and Younes Noorollahi et al. [21] relies exclusively on the standard k-ε model. Conversely, Ehsan Gholamalizadeh et al. [22] performed a three-dimensional simulation using the RNG k-ε turbulence closure, while S. Montelpare et al. [23] opted for the Realizable variant of the k-ε model. The literature reveals that the majority of researchers examine various geometric configurations using a single turbulence model without performing comparative tests with other models. The synergistic combination of solar chimney power plants (SCPPs) with other technological applications is emerging as a multifunctional strategy with high potential. Integrating the system with brackish water desalination processes (Zuo et al. [24]) would allow the use of residual heat to produce drinking water. At the same time, its coupling with agricultural drying [25] would offer an energy-efficient solution for food preservation, while its use in urban air purification [26] could capture polluting particles via the upward airflows generated by the chimney. From a climate perspective [27], the ability of SCPPs to sequester CO_2 and reduce the carbon footprint of buildings, thanks to low-energy hybrid heating and ventilation systems strengthen their role in the fight against global warming [28]. This versatility, combining clean energy production and ecosystems services, positions SCPPs as key technological platforms for a holistic energy transition.

The objective of this numerical study is to analyze the performance of a solar chimney (SCPP) by coupling accurate modeling of turbulent flows with a systematic optimization of its geometric parameters. Through numerical simulations, the emphasis is placed on the choice of an appropriate and non-random turbulence model in order to faithfully capture the thermal and dynamic phenomena within the system. This rigorous approach makes it possible to identify and quantify the impact of geometric parameters (chimney height and radius, inclination angle, etc.) on overall energy efficiency while determining the optimal configurations to maximize thermal draft and energy production..

II. NUMERICAL MEHOD

II.1 MODEL CONFIGURATION

The structure studied is a solar chimney similar to that of the Manzanares power plant [1], with a spatial organization that reflects its fundamental characteristics. Although its main dimensions correspond to those of the original model — height and radius of the chimney, and height and radius of the collector, as illustrated in Figure 1 — a notable modification was made: the collector, initially horizontal, was inclined at an angle of 1.01°. This inclination creates a distinct structural dynamic, reinforced by the conical junction connecting the ceiling to the central tower. This junction, in the form of a nozzle, aims to maximize the thermal draft by promoting a progressive acceleration of the hot air flow while minimizing pressure losses.

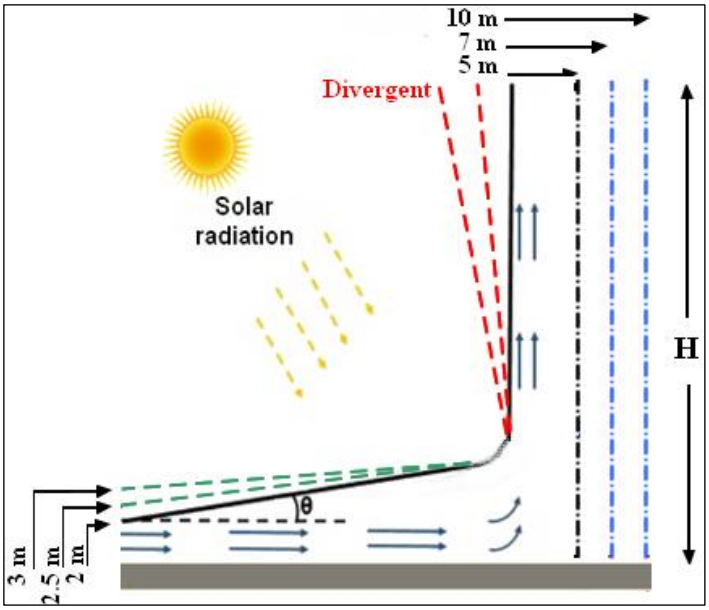

Figure 1: Solar chimney with sloped collector.
Source: Authors, (2025).

The structure preserves dimensional consistency with the reference model, while incorporating functional modifications. The chimney heights (H) range from 200 to 300 m, with diverging outlet radii of 5 to 10 m corresponding to respective inclinations of 0 to 1.43 degrees, as shown in red. The chimney radii (R_{ch}), shown in blue, vary from 5 to 10 m. The collector inlet height (H_{col}), marked in green, is between 2 and 3 m while maintaining a constant radius for the collector (R).

II.2. NUMERICAL MODELING

The airflow inside the solar chimney is characterized using the Cartesian coordinate system, considering the Boussinesq principle. According to this principle in heat transfer, it is assumed that the density of a fluid varies only with temperature, and not with pressure or other variables. This implies that the density variation of the fluid due to temperature difference is negligible compared to its mean values to simplify the fundamental equations of natural convection that occurs when temperature gradients are present. This simplification greatly simplifies the mathematical equations used to describe fluid flow, making the analysis more manageable. The governing equations governing the steady turbulent flow of an incompressible Newtonian fluid within the considered solar setup are as stated below:

a - Continuity equation

The continuity equation translating the principle of conservation of mass is:

$$\frac{\partial u_i}{\partial x_i} = 0 \tag{1}$$

b - Momentum equations

The momentum conservation equations are written as follows for i = 1, 2, and 3:

$$u_j \frac{\partial u_i}{\partial x_j} = -\frac{1}{\rho}\frac{\partial p}{\partial x_i} + \frac{1}{\rho}\frac{\partial}{\partial x_j}\left(\mu \frac{\partial u_i}{\partial x_j}\right) \tag{2}$$

c - Energy equation

The energy equation neglecting viscous dissipation is:

$$\frac{\partial (u_j T)}{\partial x_j} = \frac{\partial}{\partial x_j}\left(\alpha \frac{\partial T}{\partial x_j}\right) \tag{3}$$

The Navier-Stokes equations being non-linear, the averaging operation reveals new terms which reflect the influence of turbulence on the average flow. The system to be solved then has more unknowns than equations; hence the need to use closure models to close it. Generally, closure methods are classified based on the number of additional equations to solve. All Reynolds-Averaged Navier Stokes (RANS) models aim to determine the components of the Reynolds tensor, or Reynolds tensions to determine the average pressure and velocity. A commonly employed approach involves the application of the Boussinesq hypothesis to establish a connection between the Reynolds stresses and the mean velocity gradients. The RANS models used in our study are the first order Standard k−ε , RNG k-ε, Realizable k-ε models which use algebraic relationships to directly model the Reynolds tensor and the second order RSM (Reynolds Stress Model) which solves transport equations on Reynolds stresses.

II.2.1 STANDARD k-ε MODEL

The standard k-ε model uses the eddy viscosity hypothesis to model the Reynolds stress tensor. It consists of two equations that provide a comprehensive overview of turbulence through the use of two supplementary transport equations,, one for the turbulence kinetic energy (k) and one for the turbulence dissipation rate (ε). The two equations are obtained from the following transport equations:

$$\frac{\partial}{\partial t}(\rho k) + \frac{\partial}{\partial x_i}(\rho k u_i) = \frac{\partial}{\partial x_i}\left[\left(\mu + \frac{\mu_k}{\sigma_k}\right)\right] + G_k + G_b - \rho\varepsilon - Y_M + S_k \quad (4)$$

$$\frac{\partial}{\partial t}(\rho \varepsilon) + \frac{\partial}{\partial x_i}(\rho \varepsilon u_i) = \frac{\partial}{\partial x_i}\left[\left(\mu + \frac{\mu_t}{\sigma_\varepsilon}\right) + \frac{\partial \varepsilon}{\partial x_j}\right] + C_{1\varepsilon}\frac{\varepsilon}{k}(G_k + C_{3\varepsilon}G_b) - C_{2\varepsilon}\rho\frac{\varepsilon^2}{k} + S_\varepsilon \quad (5)$$

G_k is a measure of the production of k, illustrating the transfer of energy from mean motion to turbulence, under the influence of Reynolds stresses. G_b indicates the contribution of buoyancy to the creation or destruction of k, related to gravity and thermal gradients. S_k and S_ε are source terms. Y_M refers to the dissipation of k due to expansion, which can be considered negligible in an incompressible context. The turbulent Prandtl numbers σ_k and σ_ε govern the diffusion of k and ε. The coefficients $C_{1\varepsilon}$ and $C_{2\varepsilon}$ control the production and destruction of ε, while $C_{3\varepsilon}$ adjusts the effect of buoyancy on ε. The turbulent viscosity μ_t is calculated as follows:

$$\mu_t = \rho\, C_\mu \frac{k^2}{\varepsilon} \quad (6)$$

$$G_k = \mu_t S^2 \quad (7)$$

$$S = \sqrt{2 S_{ij} S_{ij}} \quad (8)$$

$$S_{ij} = \frac{1}{2}\left(\frac{\partial u_j}{\partial x_i} + \frac{\partial u_i}{\partial x_j}\right) \quad (9)$$

The constants of this model are:

$\sigma_k = 1;\ \sigma_\varepsilon = 1.3;\ C_{1\varepsilon}$=1.44; $C_{2\varepsilon}$=1.92; C_μ=0.09

II.2.2 RNG k-ε MODEL

The RNG k-ε turbulence model is an improved version of the standard k-ε model, analytically developed from the instantaneous Navier-Stokes equations through the application of the renormalization group (RNG) technique. This mathematical approach allows for the effects of unresolved turbulent scales to be taken into account via a systematic averaging process, unlike the standard model whose constants are empirically calibrated.

$$\frac{\partial}{\partial t}(\rho k) + \frac{\partial}{\partial x_i}(\rho k u_i) = \frac{\partial}{\partial x_j}\left(\alpha_k \mu_{eff}\frac{\partial k}{\partial x_j}\right) + G_k + G_b - \rho\varepsilon - Y_M + S_k \quad (10)$$

$$\frac{\partial}{\partial t}(\rho \varepsilon) + \frac{\partial}{\partial x_i}(\rho \varepsilon u_i) = \frac{\partial}{\partial x_j}\left(\alpha_\varepsilon \mu_{eff}\frac{\partial \varepsilon}{\partial x_j}\right) + C_{1\varepsilon}\frac{\varepsilon}{k}(G_k + C_{3\varepsilon}G_b) - C_{2\varepsilon}\rho\frac{\varepsilon^2}{k} - R_\varepsilon + S_\varepsilon \quad (11)$$

The constants identified in the model are not the same as those in the standard k-ε model:

$\alpha_k = \alpha_\varepsilon \simeq 1.393$; $C_{1\varepsilon}$=1.42 ; $C_{2\varepsilon}$=1.68.

II.2.3 REALIZABLE k-ε MODEL

The realizable k-ε turbulence model is an evolution of the standard k-ε model, designed to improve accuracy in complex flows by ensuring physically realizable turbulent stresses, i.e., that the normal turbulence stresses remain positive. The transport equations are:

$$\frac{\partial}{\partial t}(\rho k) + \frac{\partial}{\partial x_j}(\rho k u_j) = \frac{\partial}{\partial x_j}\left[\left(\mu + \frac{\mu_t}{\sigma_k}\right)\frac{\partial k}{\partial x_j}\right] + G_k + G_b - \rho\varepsilon - Y_M + S_k \quad (12)$$

$$\frac{\partial}{\partial t}(\rho \varepsilon) + \frac{\partial}{\partial x_j}(\rho \varepsilon \mu_j) = \frac{\partial}{\partial x_j}\left[\left(\mu + \frac{\mu_t}{\sigma_\varepsilon}\right)\frac{\partial \varepsilon}{\partial x_j}\right] + \rho C_1 S\varepsilon - \rho C_2 \frac{\varepsilon^2}{k + \sqrt{\upsilon\varepsilon}} + C_{1\varepsilon}\frac{\varepsilon}{k}C_{3\varepsilon}G_b + S_\varepsilon \quad (13)$$

where:

$$C_1 = \max\left[0.43, \frac{\eta}{\eta+5}\right] \quad (14)$$

$$\eta = S\frac{k}{\varepsilon} \quad (15)$$

In order to ensure optimal performance of this turbulence model for certain canonical flows (Channel Flow, free jet, etc.), the constants C_2, σ_k and σ_ε have been determined. The values of these constants are as follows:

$C_{1\varepsilon} = 1.44;\ C_2 = 1.9\ ;\ \sigma_\varepsilon = 1.2\ ;\ \sigma_k = 1$

Buoyancy influences ε, which is defined by the constant $C_{3\varepsilon}$. In Fluent, this constant is not provided, but is determined by the following formula:

$$C_{3\varepsilon} = tanh\left|\frac{v}{u}\right| \quad (16)$$

The flow velocity is decomposed into two components: v, parallel to the gravitational vector, and u, perpendicular to it. Therefore, $C_{3\varepsilon}$ takes the value 1 for buoyant shear layers whose main flow follows the direction of gravity. Conversely, $C_{3\varepsilon}$ becomes zero for buoyant shear layers perpendicular to the gravitational vector.

II.2.4 RSM TURBULENCE MODEL

The RSM model takes a different approach within RANS approach. Instead of relying on the eddy viscosity assumption, RSM solves transport equations for each individual component of the Reynolds Stress Tensor directly. The modeled transport equations for k and ε in the RSM model are:

$$\frac{\partial}{\partial t}(\rho k) + \frac{\partial}{\partial x_i}(\rho k u_i) = \frac{\partial}{\partial x_j}\left[\left(\mu + \frac{\mu_t}{\sigma_k}\right)\frac{\partial k}{\partial x_j}\right] + \frac{1}{2}(G_{ii} + P_{ii}) - \rho\varepsilon(1 + 2M_t^2) + S_k \quad (17)$$

$$\frac{\partial}{\partial t}(\rho \varepsilon) + \frac{\partial}{\partial x_i}(\rho \varepsilon \mu_i) = \frac{\partial}{\partial x_j}\left[\left(\mu + \frac{\mu_t}{\sigma_\varepsilon}\right)\frac{\partial \varepsilon}{\partial x_j}\right] C_{\varepsilon 1}\frac{1}{2}[Pii + C_{\varepsilon 3}G_{ii}]\frac{\varepsilon}{k} - C_{\varepsilon 2}\rho\frac{\varepsilon^2}{k} + S_\varepsilon \quad (18)$$

Where, $\sigma_k = 0.82$, $\sigma_\varepsilon = 1.0$, $C_{\varepsilon 1} = 1.44$, $C_{\varepsilon 2} = 1.92$, $C_{\varepsilon 3}$ is evaluated as a function of the local flow direction relative to the gravitational vector, and S_k and S_ε are a user-defined source terms. M_t is the turbulent Mach number. G_{ii} is the production terms due to buoyancy. P_{ii} is the stress production.

III. POWER GENERATION

The performance of a chimney solar power plant relies on optimal synergy between its key components, forming an interdependent system where each element plays a critical role. The solar collector, by converting radiation into heat, generates an upward flow of hot air. This thermal energy is then amplified by the chimney effect, which accelerates natural convection thanks to the difference in density between the hot air and the atmosphere. The turbine, strategically positioned at the base of the chimney, finally transforms this kinetic energy into electricity. A failure or undersizing of one of these elements leads to a drop in energy production. Thus, system optimization requires precise modeling of the physical parameters of each component: collector surface area, model or height of the chimney, and electrical power generated by the turbine. The performance of a chimney solar power plant depends in a complex way on the efficiency of each component, which can be expressed by the mathematical formulas specific to each of them.

III.1 THE SOLAR COLLECTOR

The efficiency of the collector is of utmost importance in chimney solar power plants as it directly impacts the overall performance and electricity generation capacity of these systems. The efficiency of collector is given by:

$$\eta_{coll} = \frac{\dot{Q}}{A_{coll}.G} \quad (19)$$

The generated heat $\dot{Q}$ and the mass flow rate $\dot{m}$ are provided as follows:

$$\dot{Q} = \dot{m}.C_p.\Delta T \quad (20)$$

$$\dot{m} = \rho_{coll}.V_c.A_c \quad (21)$$

Where, ΔT is the temperature difference between the heated air under the collector and the ambient air (K).
By substituting in Equation 19, $\dot{Q}$ and $\dot{m}$ by their expressions, we obtain the relation:

$$\eta_{coll} = \frac{\rho_{coll}.V_c.A_c.C_p.\Delta T}{A_{coll}.G} \quad (22)$$

III.2 THE SOLAR CHIMNEY

The efficiency of the chimney is expressed according to Ref [1] by:

$$\eta_{sc} = \frac{g.H_{sc}}{C_p.T_0} \quad (23)$$

The calculation of the pressure difference generated by the chimney is performed as follows:

$$\Delta p_{tot} = \rho_{coll}.g.H_{sc}\frac{\Delta T}{T_0} \quad (24)$$

III.3 THE TURBINE

The Solar chimney system turbine belongs to a pressure-based wind turbine. The front and rear air velocities are almost the same, but the pressure changes significantly. The output power is given by:

$$P = x\sqrt{1-x}.\eta_{coll}.\eta_{wt}.\left(\frac{g}{C_p\,T_0}\right).H_{sc}.A_{coll}.G \quad (25)$$

The maximum output power of the system is achieved when the turbine pressure drop factor (x) is set to 2/3. Meanwhile, in this study, the turbine efficiency (η_{wt}) was established to 80 %.

IV. BOUNDARY CONDITIONS

The geometric model of the chimney with sloped roof considered in our study presents a notable similarity to the scenario of the SCPP of Manzanares. The boundary conditions for the simulation of the solar collector are specified according to the highest solar radiation in the Constantine region which is approximately 960 W [29]. The collector inlet and chimney outlet are characterized by their

respective inlet and outlet pressure limits, which are set at 0 Pa, while axisymmetric conditions were implemented at the center of the device. The chimney wall is considered an adiabatic boundary. The environmental temperature is set at 298 K. The bottom of the energy storage layer is set as a constant temperature boundary, with the temperature set at 300 K. Finally, the 1.01° inclined collector roof takes into account the convection limits with a coefficient set at 9.5 W/(m^{2}K), suitable for low ambient air velocities. At a temperature of 25 °C, Table 1 shows the thermophysical properties of air. The boundary conditions for different locations are shown in detail in Table 1.

Table 1: Thermophysical properties of air at 25 °C.

Fluid	ρ (kg/m^3)	k (W/m.K)	μ (kg/m.s)	C_p (J/kg.K)
Air	1.184	0.0255	1.849 10^{-5}	1007

Source: [20].

The governing equations for flow and energy (Equations (1)–(10)) are solved numerically under the specified boundary conditions shown in Table 2, using the commercial code Ansys Fluent, which employs a finite volume method.

Table 2. Boundary conditions.

Surface	Type	Value
Collector roof	Wall	Mixed; T_{ext} = 300 K, h_s = 9.5 W/m^{2}K,
wall surface	Wall	Adiabatic; $qch = 0\ W/m^2$
Ground	Wall	G = 960 W/m^2
Inlet of collector	Pressure-inlet	T_{ext} = 302 K, p_{gauge} = 0 Pa
Outlet of chimney	Pressure-outlet	T_{ext} = 300 K, p_{gauge} = 0 Pa

Source: Authors, (2025).

The geometry is designed and meshed with Gambit software 2.4.6. To jointly solve the continuity, momentum, and pressure equations, the SIMPLE (Semi-Implicit Method for Pressure-Linked Equations) algorithm, based on pressure-velocity coupling, is used. The convective terms of the momentum and energy transport equations are discretized using a power law scheme. The discrete ordinate (DO) model was chosen to solve the radiative transfer equation (RTE) in the modeling of radiation heat transfer phenomena. To maintain numerical stability, under-relaxation factors are applied during the iteration of the discretized equations. The convergence criterion is set at 10^{-5} for the mass and momentum equations, and at 10^{-6} for the energy equation.

V. RESULTS AND DISCUSSION

V.1 ANALYSIS OF MESH SENSITIVITY

The precision of the calculation and the overall accuracy of numerical simulation results are influenced by the type and size of the grid. Conducting grid-independent analysis allows for the determination of a grid density that is appropriate for the specific problem, thereby ensuring the accuracy of the results. To reduce the mesh requirements, wall laws are implemented to connect turbulent variables, such as k and ε, with wall conditions. All the turbulence models mentioned earlier are intended for use with (y+) values greater than 30, indicating that the first mesh cell must be positioned within the logarithmic region of the boundary layer, in our case (y+ > 177). A variety of uniform quadrilateral structured mesh generated (Figure 2(a)), were tested. Three mesh grids were evaluated as shown in Figure 2(b) to determine the optimal trade-off between independence results, and calculation time.

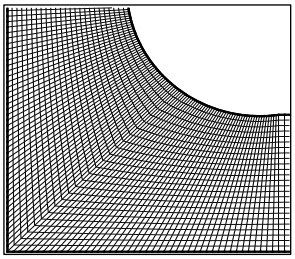

(a)

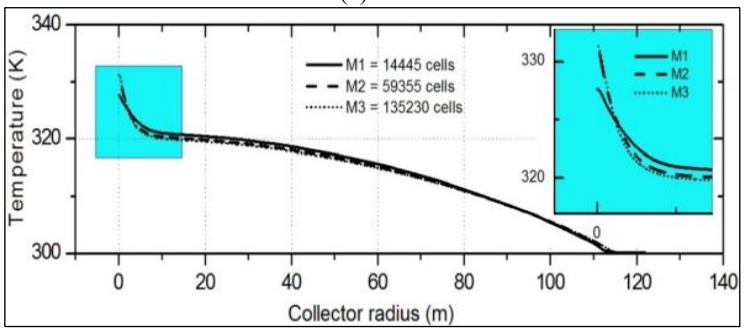

(b)

Figure 2: (a) Grid mesh and (b) mesh sensitivity analysis.
Source: Authors, (2025).

The tests carried out reveal a significant difference of the temperature curves obtained along the median radius of the collector between the M1 and M2 mesh configurations, while the M2 and M3 configurations are in perfect agreement with a minimal deviation. This demonstrates that the solution obtained is not significantly affected by the mesh resolution after the implementation of the M2 configuration, i.e. 59355 cells, indicating that it is truly representative of the physical system being simulated. Therefore, the M2 configuration was used for all simulations performed in this study.

V.2 CODE VALIDATION

Table 3 presents a comparison of our numerical results with those of Schlaich [1] for the same geometric parameters of his Manzanares solar chimney. The parameter analyzed here is the power developed by the chimney, evaluated through several distinct turbulence models. Among these models, the RNG k-ε turbulence model stands out for a better agreement with the reference data, displaying a minimum relative error of 1.32, which underlines its accuracy in predicting the dynamic behaviors of the air flow in the solar chimney. Conversely, the Standard k-ε turbulence model records the most significant deviation, with a significantly higher relative error value, indicating a poorer agreement with the expected results. These deviations highlight the critical impact of the choice of the model on the reliability of the simulations, especially for applications requiring high accuracy in terms of the electrical power of the solar chimney station.

Table 3: Comparisons between our numerical procedure and the experimental results of.

Turbulence model	H (m)	G (W/m^2)	P (kW)	P (kW) Error Relat
Standard k-ε	200	1000	52,87	5,73156
Realizable k-ε	200	1000	51,13	2,26635
RNG k-ε	200	1000	49,34	1,31928
RSM	200	1000	49,05	1,9
Experimental (Schlaich)	200	1000	50	

Source: [1]

V.3 TURBULENCE MODEL EFFECT

Figure 3 illustrates the velocity contours obtained under the specified boundary conditions (G = 960 W/m^2, H = 200 m, H_{col}= 2 m, R_{ch} = 5 m), revealing a broadly similar spatial distribution among the different turbulence models. The maximum velocity is systematically located near the curved wall of the solar chimney, highlighting a concentration of dynamic effects in this area.

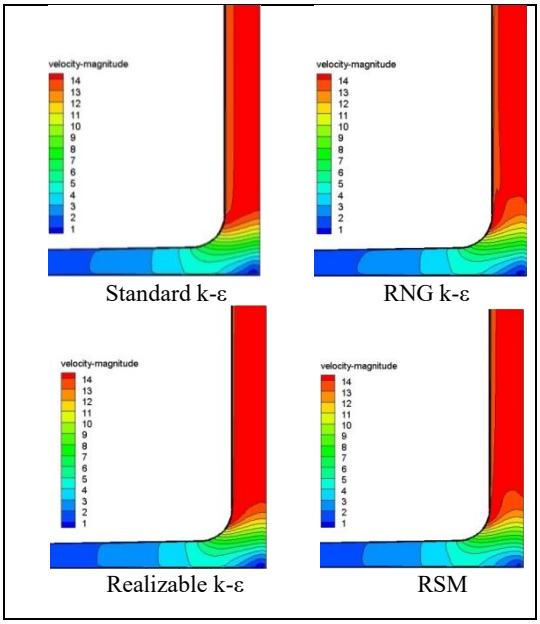

Figure 3: Velocity contours (H_{col}= 2 m, R_{ch} = 5m).
Source: Authors, (2025).

However, when examining the velocity profiles at the tower inlet, Figure 4(a) reveals a notable disparity in the velocity distribution near the wall. Moreover, the velocity separation occurs earlier with the Standard k-ε turbulence model than with the other models. The maximum recorded velocity values differ significantly: 13.98 m/s for the Standard k-ε model, 13.78 m/s for the Realizable k-ε model, 13.51 m/s for the RNG k-ε model and 13.48 m/s for the RSM model. These deviations are summarized in Figure 4(b), which compares the velocity differences between the models, showing that the Standard k-ε model presents the highest difference compared to the adequate RNG k-ε model. This highlights the impact of the modeling choices on the velocity distribution in the structure. However, the RNG k-ε model remains the one closest to the RSM model, which recorded a difference of only 0.03 m/s. It is noted that the flow separation near the curved wall upstream of the chimney tower, observed in particular with the Standard k-ε model, constitutes a critical phenomenon directly influencing the overall performance and stability of the flow. An early separation, such as that predicted by this model, can generate turbulent recirculation zones, amplifying pressure losses and degrading the energy efficiency of the system.

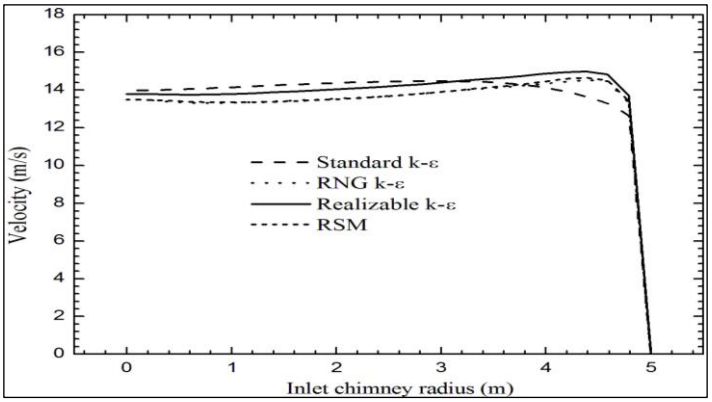

(a)

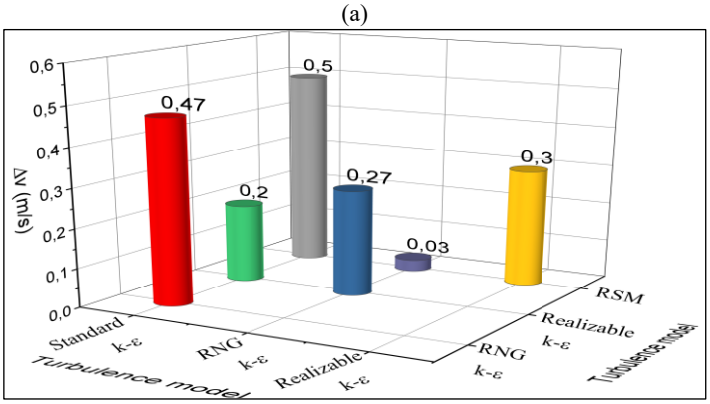

(b)

Figure 4: (a) Velocity profiles and (b) the maximum velocity difference between turbulence models.
Source: Authors, (2025).

To assess the ability of turbulence models to capture and reproduce turbulence in the flow inside the solar chimney, Figure 5 shows the distribution of turbulent kinetic energy, which represents the energy associated with velocity fluctuations in the turbulent flow. As hot air rises in the chimney, it is subjected to a significant velocity gradient between the main (fast) flow and the slower-moving air in contact with the walls. This intense shear generates instabilities and promotes turbulence production, thus increasing the turbulent kinetic energy near the walls. The distribution of the high turbulent kinetic energy region differs among the turbulence models. The results obtained from the three models, namely Standard k-ε, RNG k-ε, and Realizable k-ε, present a region of intense turbulence near the chimney wall downstream of the bend. However, the RSM model indicates that this region is located in the middle of the chimney tower inlet.

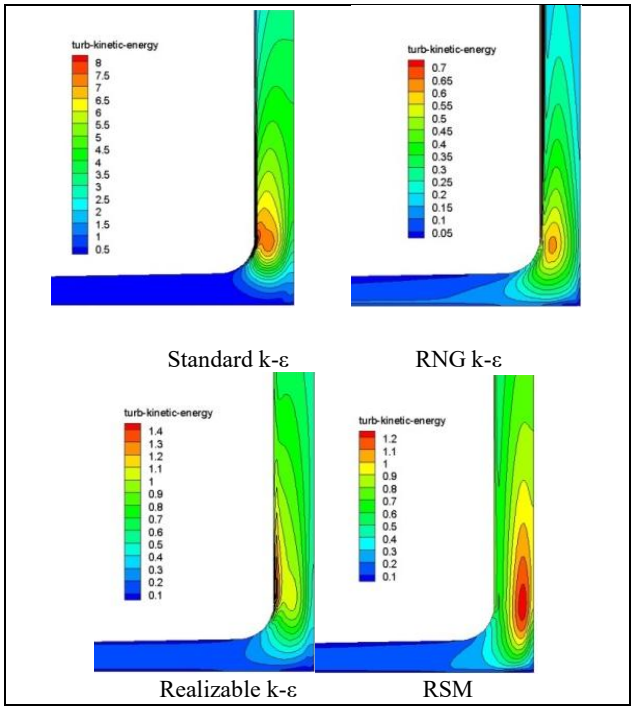

Figure 5: Contours of turbulent kinetic energy (H_{col}= 2 m, R_{ch} = 5m).
Source: Authors, (2025).

Figure 6(a) better illustrates this difference interpreted by the turbulent kinetic energy profiles along the radius just at the chimney tower inlet.

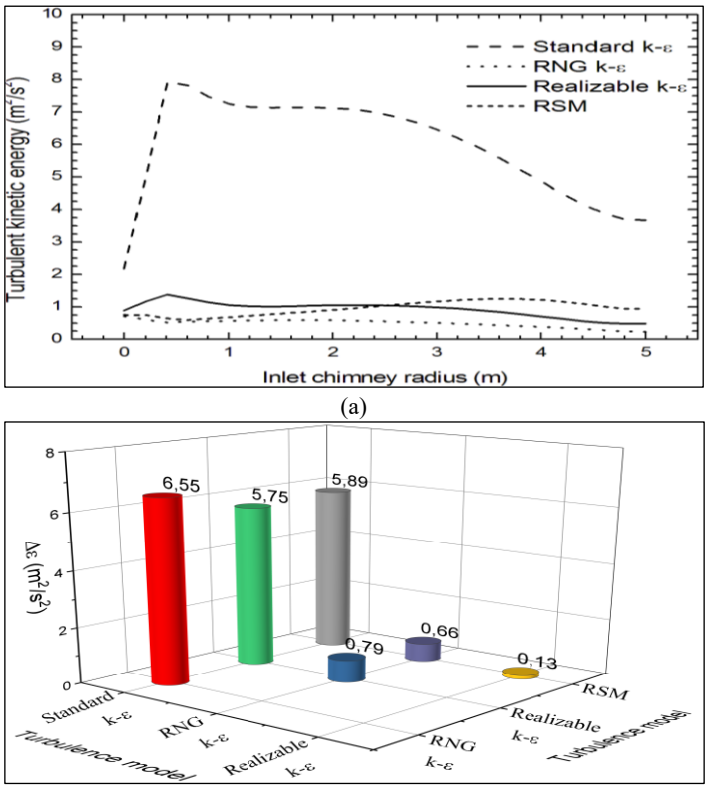

Figure 6: (a) Turbulent kinetic energy profiles and (b) the maximum turbulent kinetic energy difference between turbulence models.
Source: Authors, (2025).

Figure 6(a) better illustrates this difference interpreted by the turbulent kinetic energy profiles along the radius just at the chimney tower inlet. The standard k-ε model overestimated the turbulent kinetic energy throughout the section near the stagnation point by a maximum value of 7.14 m^2/s^2. The RNG k-ε model identified a zone of lowest turbulence with a maximum value of 0.59 m^2/s^2.

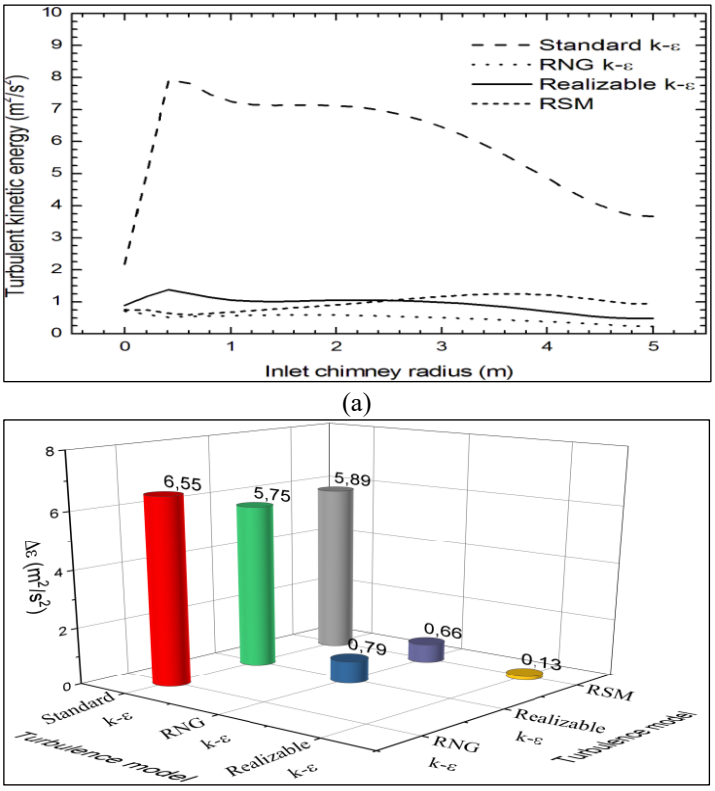

Figure 6: (a) Turbulent kinetic energy profiles and (b) the maximum turbulent kinetic energy difference between turbulence models
Source: Authors, (2025).

The RSM model, however, predicted an intensification of the vortex flow in the middle of the chimney with a maximum value of 1.25 m^2/s^2, which was lower than the value recorded by the Realizable k-ε model near the chimney wall, which was 1.38 m^2/s^2. The difference in the maximum value of turbulent kinetic energy among the four models can be observed in Figure 6(b). Moreover, the three two-equation turbulence models, Standard k-ε, RNG k-ε and Realizable k-ε predicted a decreasing intensification of the wall kinetic energy in the middle of the chimney in contrast to the increasing evolution marked by the seven-equation RSM turbulence model.

Figure 7 illustrates the temperature distribution along the solar chimney for different turbulence models. The results indicate that the temperature field is mainly concentrated in the middle of the solar chimney, extending from the collector outlet to the top of the chimney tower. Warmer and less dense air rises along the central axis of the tower, while colder and denser air descends along the walls. This movement generates an upward flow of hot air in the middle of the chimney, which transports the heat to the highest part of the tower. In the confluence zone located at the base of the solar chimney, the highest temperature values were observed. This phenomenon can be attributed to the confinement effect, where the air flow converges and the space available for lateral dispersion decreases. Therefore, this can lead to the accumulation of hot air and an increase in pressure in this region. All four turbulence models successfully captured the natural convection phenomenon, although there were discrepancies in terms of spatial distribution and temperature values. The choice of turbulence model also had an impact on the temperature distribution.

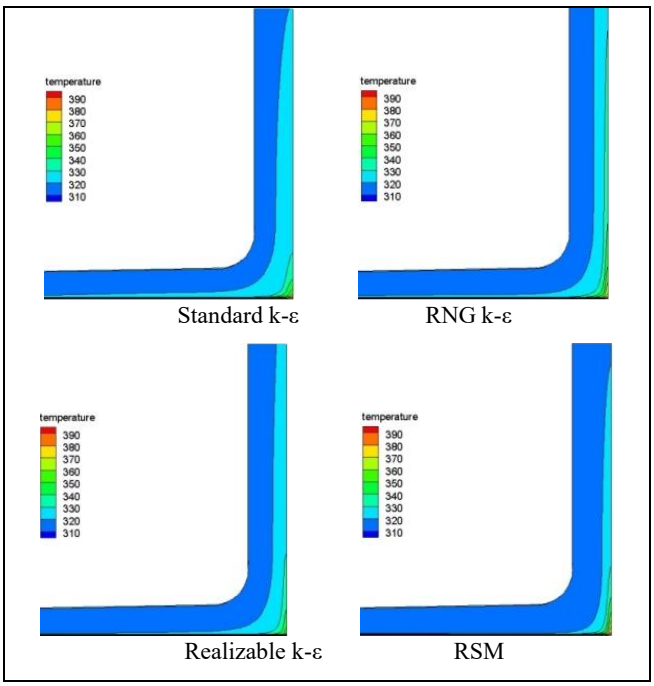

Figure 7: Contours of temperature (H_{col}= 2 m, R_{ch} = 5m).
Source: Authors, (2025).

Figure 8(a) illustrates the temperature profiles along the chimney inlet radius, revealing variations in the temperature value at the chimney according to the different models. To be more precise, for the standard k-ε model, the recorded temperature was 325.71 K, while for the RNG k-ε model, it was 340.78 K. The feasible k-ε model gave a temperature of 331.89 K, and the RSM model gave a temperature of 329.81 K. The maximum temperature difference among the four models was 15.07 K, as illustrated in Figure 8(b).

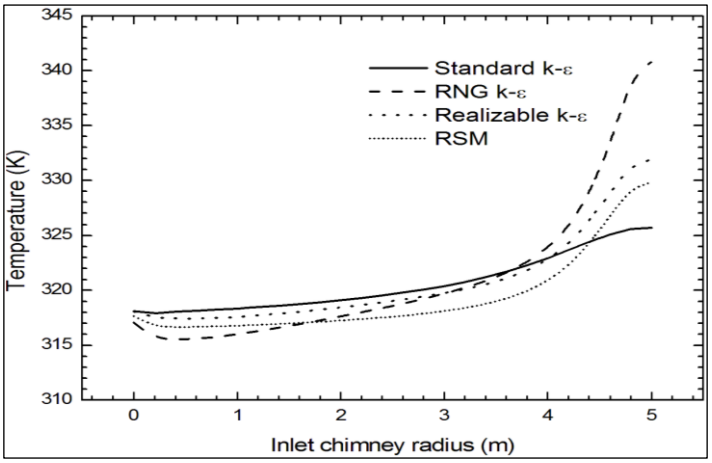

(a)

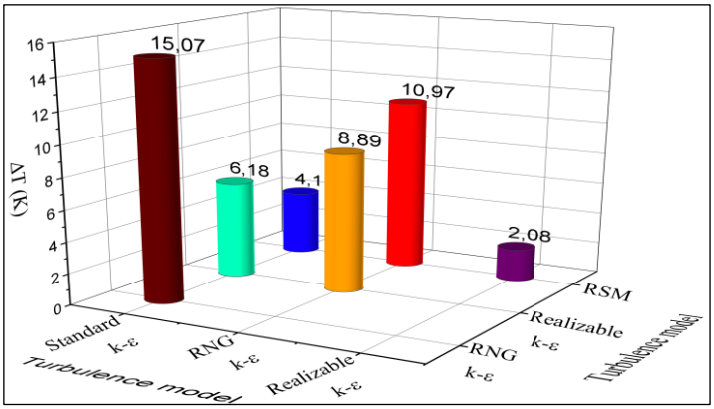

(b)

Figure 8: (a) Temperature profiles and (b) the maximum temperature difference between turbulence models.
Source: Authors, (2025).

V.4 CHIMNEY HEIGHT EFFECT

Figure 9 illustrates columns of power and mass flow rate, simulated under identical boundary conditions (G = 960 W/m^2, H = 200 m, Rcol= 2 m, Rch = 5 m). The analysis focuses on the influence of the chimney height (200 m, 250 m and 300 m) on these parameters. The results demonstrate that an increase in height significantly amplifies the generated power (Figures 9(a)). As the air heats up at the base of the solar chimney, it becomes less dense and naturally rises. A greater height provides more space for this hot air to move, creating a greater "thermal draft" effect. This causes the airflow to accelerate, which increases the mass flow rate (Figure 9(b)), and therefore the higher the chimney, the stronger the chimney effect, contributing to a significant increase in the power generated by the solar chimney. For example, from 200 m to 300 m, the mass flow rate increased by 173 kg/s, generating an optimal power of 75 kW. A higher mass flow rate increases the kinetic energy available for power production (via a turbine), thus improving energy conversion efficiency.

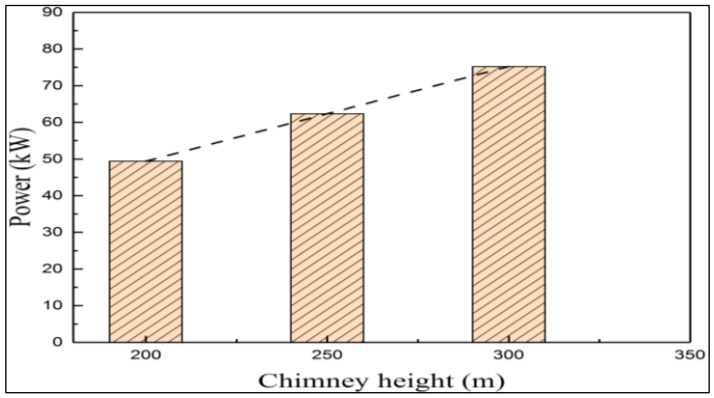

(a)

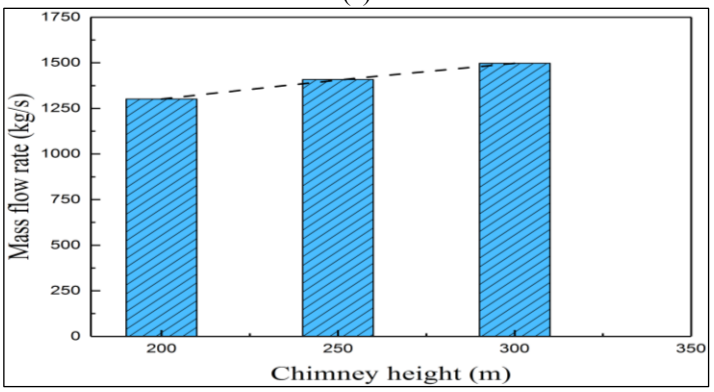

(b)

Figure 9: (a) Height of chimney effect on: (a) output power plant and (b) mass flow rate.
Source: Authors, (2025).

Figure 10 illustrates the relationship between chimney height and gas flow velocity. Three separate curves show this relationship for initial chimney heights of 200, 250, and 300 m. A rapid increase in gas velocity is observed with increasing chimney height. This trend is explained by the reduction in flow resistance offered by a taller chimney, thus facilitating gas flow. However, this increase is not linear and reaches a plateau, indicating that the velocity stabilizes beyond a certain height. The increase in air velocity, although always positive, becomes increasingly smaller with increasing chimney height, suggesting the existence of a limit to the velocity improvement.

Near the curved wall of the chimney for all three different heights, the maximum air velocity accelerates due to the centrifugal force pushing the fluid outward, creating a radial pressure gradient. Secondary flows redistribute momentum by directing the fast-moving fluid from the center toward the wall, while turbulence locally reduces the boundary layer thickness. The velocity reaches its maximum just nearby, where these effects combine. Note that the position of the turbine in the solar chimney is crucial, as shown in Figures 10 (a,b). It plays a key role in optimal energy production. This production closely depends on the maximum air velocity. It is necessary to adjust the turbine location according to this velocity. In our case, the ideal location of the turbine is right at the entrance of the solar chimney tower. This location remains the same for all heights considered.

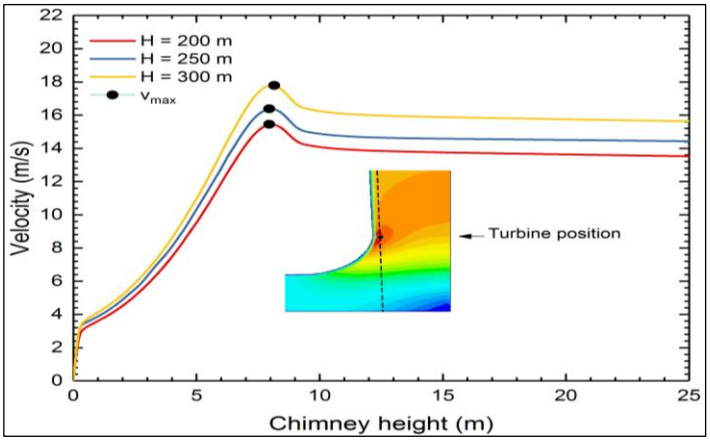

(a)

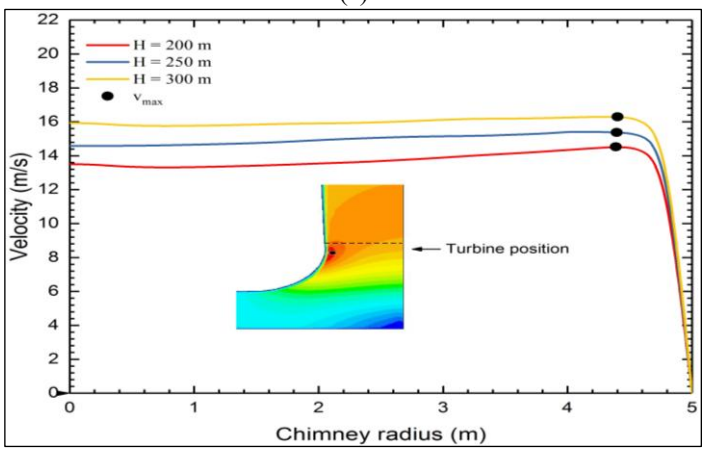

(b)

Figure 10: (a) Velocity profiles : (x =0.5 m) and (b) Chimney inlet (y = 9 m).
Source: Authors, (2025).

When the height of a chimney increases, two main effects occur at the collector outlet, linked to the principles of thermodynamics as illustrated in Figure 11: The increase in velocity and the decrease in temperature. The increase in velocity results from the natural draft caused by Archimedes' thrust, the effect of which increases with height (Figure 11(a)). This thrust, directly proportional to the height, is transformed into kinetic energy by the application of Bernoulli's principle, thus leading to an increase in the velocity at the outlet.

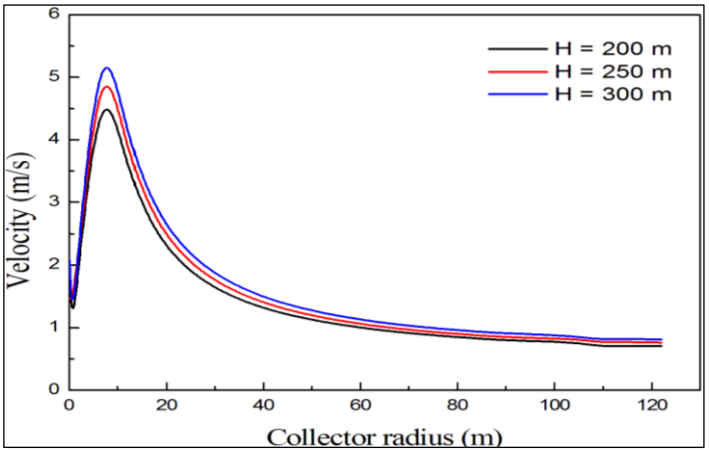

(a)

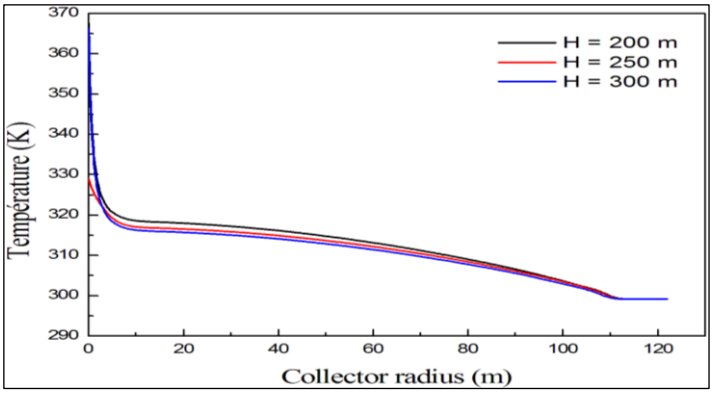

(b)

Figure 11: Height of chimney effect on: (a) velocity and (b) temperature.
Source: Authors, (2025).

Furthermore, the decrease in outlet temperature, imposed by relation (20) due to the constant radiated power, is associated with the increase in height (Figure 11(b)). This leads to a higher mass flow rate, because the system draws in more air to compensate for pressure differences. This combination of parameters (increased height, high mass flow rate and fixed power) mechanically leads to cooling at the outlet.

V.5 CHIMNEY DIVERGENCE ANGLE EFFECT

Similarly, Figure 12 is divided into two parts that study the relationship between the exit radius of a chimney, while keeping the inlet radius constant at 5 m, and the two separate variables: gas flow rate and power. The first part of the graph, on the left (Figure 12(a)), examines power as a function of chimney radius. Unlike flow rate, power shows a much weaker relationship with chimney radius. A slight increase in power of 3.18 %, equal to 51 kW, is observed when the chimney exit radius is extended from 5 m to 10 m, corresponding to a diverging flue angle of 1.43°. However, this increase remains negligible compared to the increase in flow rate.

The second part, on the right (Figure 12(b)), shows the gas mass flow rate as a function of chimney radius. It is observed that as the chimney radius increases, the gas flow rate also increases. This increase is not linear, but rather an upward curve. When the chimney exit radius increases from 5 m to 10 m (diverging angle from 0° to 1.43°), the rate of increase in flow rate reaches 95 %. This can be explained by the fact that a larger exit radius provides a larger cross-sectional area for gas flow, thus reducing resistance and allowing a higher flow rate. This suggests that, although increasing the chimney radius significantly improves gas flow, its impact on power is relatively small. This may be due to the fact that power depends on several factors, including gas pressure, which may not increase proportionally with chimney radius.

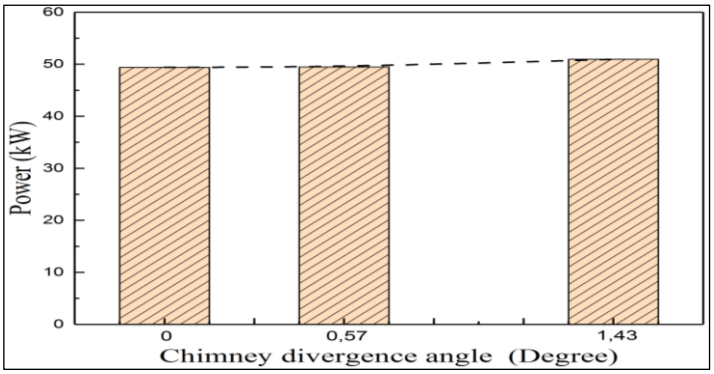

(a)

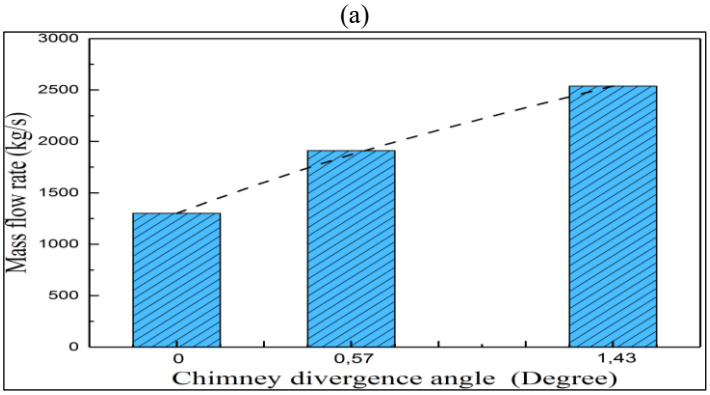

(b)

Figure 12: Chimney divergence angle effect on: (a) output power plant and (b) mass flow rate.
Source: Authors, (2025).

Increasing the divergence angle of the solar tower (i.e., broadening its shape), as illustrated in Figure 13, acts on the system in a similar way to increased height, amplifying two key effects: increased velocity(Figure 13(a)) and decreased temperature(Figure 13(b)) at the collector outlet. A more open divergence angle prolongs the chimney effect by creating a more pronounced vertical pressure gradient. A divergent angle reduces dynamic pressure losses by progressively widening the tower section, which promotes continuous acceleration of the fluid. To respect energy conservation, an increase in mass flow rate necessarily requires a reduction in the temperature difference, and therefore a lower outlet temperature.

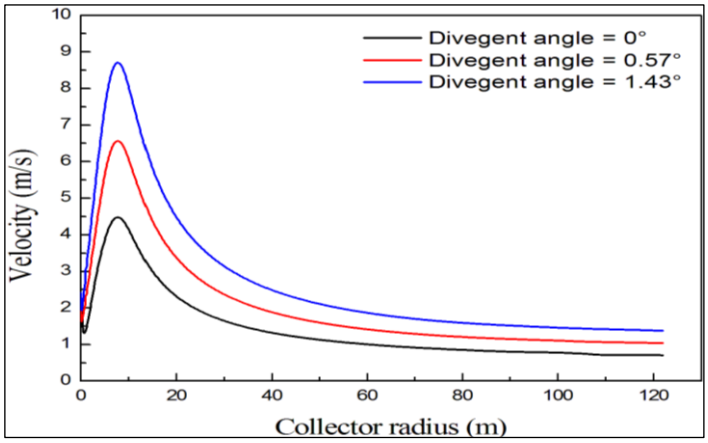

(a)

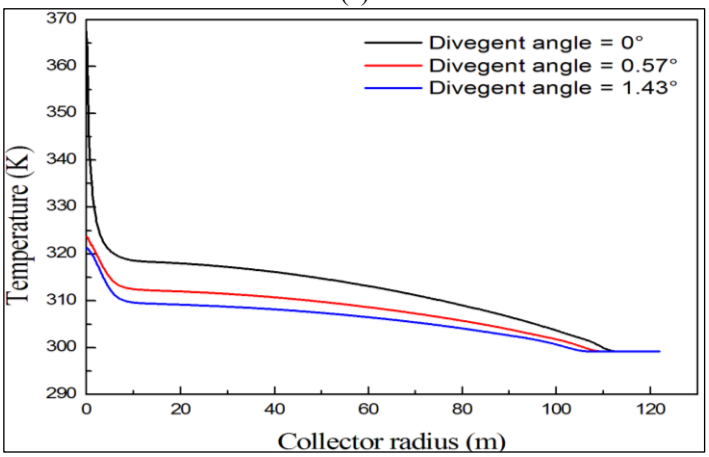

(b)

Figure 13. Chimney divergence angle effect on: (a) velocity and (b) temperature
Source: Authors, (2025).

V.6 CHIMNEY RADIUS EFFECT

Figure 14 highlights the decisive impact of the chimney wall profile on the flow characteristics and, consequently, on the output power and flow rate generated by the plant. A marked positive correlation is observed between the chimney radius and the generated power, following a polynomial trend (Figure 14(a)).

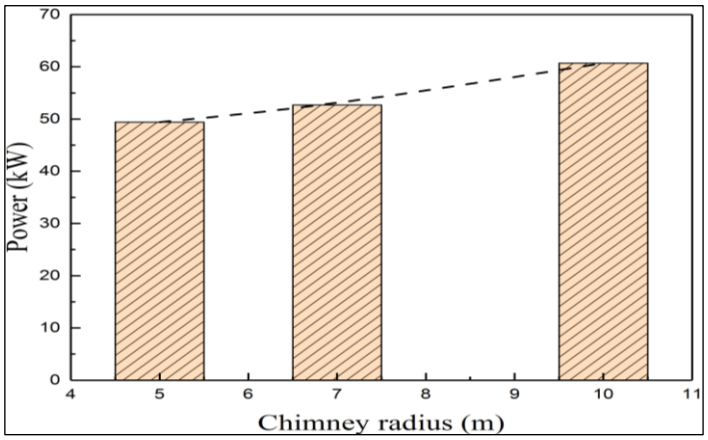

(a)

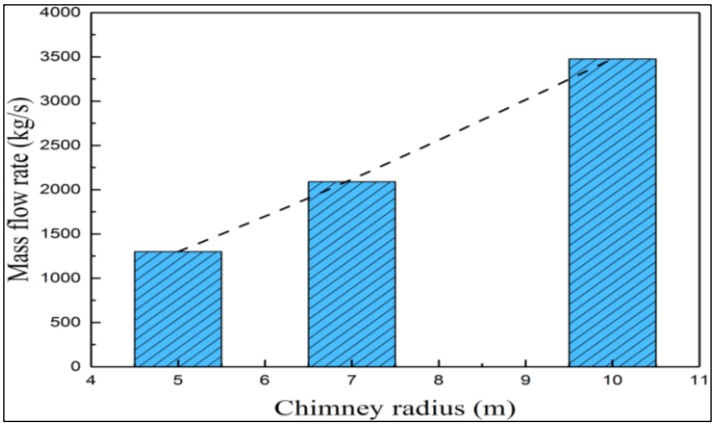

(b)

Figure 14: (a) Chimney radius effect on: (a) output power plant and (b) mass flow rate
Source: Authors, (2025).

For radii between 5 and 7 m, the power progression remains gradual from 49.4 kW to 52.69 kW. Beyond 7 m, this growth intensifies significantly, indicating that the positive effects related to widening then outweigh the potential constraints. According to the curve, an optimal power of 60.7 kW is achieved for a uniform chimney radius of 10 m, with an increase rate of 22.89 %. At this threshold, the transformation of thermal energy into kinetic energy is maximized thanks to an increased air flow and a reduction in turbulence. This nonlinear dynamic thus highlights the acceleration of performance as a function of the radius scale. In terms of mass flow rate, Figure 14(b) reveals a strong positive correlation between the radius of the chimney and that of its outlet, displaying respective increase gradients of 1301 kg/s and 3477 kg/s, ranging from minimum to maximum values. Increasing the uniform radius of the solar chimney (Figure 15), accelerates the air and reduces its temperature at the collector outlet via moderate adiabatic expansion, but these effects remain less pronounced than with an increased divergence angle(Figure 15(b)).

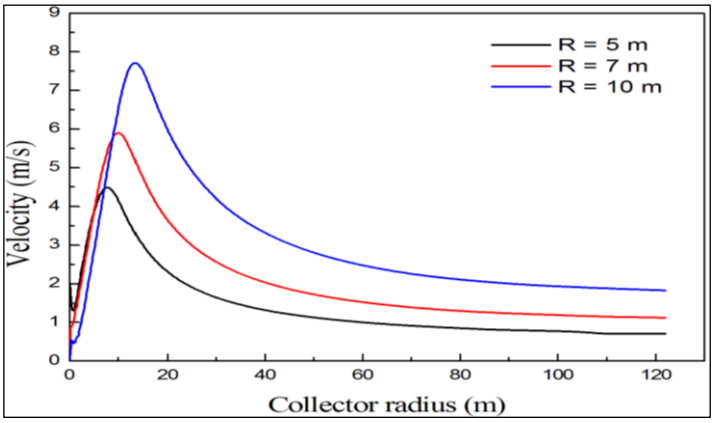

(a)

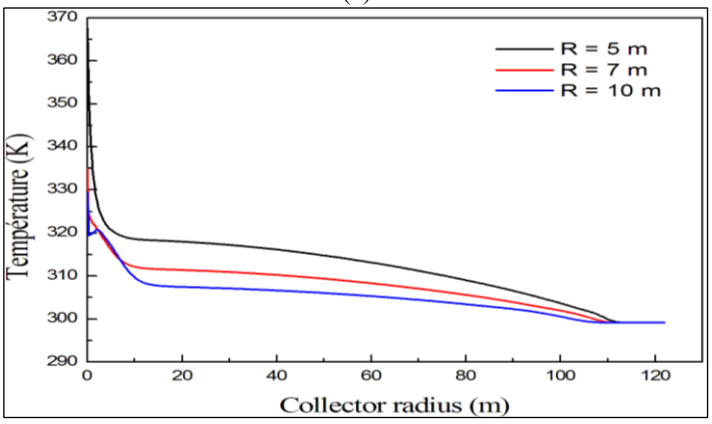

(b)

Figure 15: Chimney radius effect on: (a) velocity and (b) temperature.
Source: Authors, (2025).

The latter, by progressively widening the cross-section, amplifies the theoretical velocity (by conservation of mass and reverse Venturi effect) and further lowers the temperature thanks to a more pronounced adiabatic expansion. However, a high divergence angle generates significant pressure losses (turbulence, increased friction) that dissipate kinetic energy, limiting the effective velocity and reducing the air density. Conversely, an enlarged uniform radius preserves a stable and laminar flow, minimizing pressure losses while

maintaining a constant cross-section. This allows thermal buoyancy (linked to the density gradient) to dominate, favoring a higher mass flow rate despite lower local gains in velocity or cooling (Figure 15(a)).

V.7 INLET COLLECTOR HEIGHT EFFECT

Figure 16, a bar graph, relates the collector height to the generated power and mass flow rate under the same specified boundary conditions (G = 960 W/m^2, H = 200 m, R_{ch} = 5 m). Three vertical bars illustrate the power produced at different collector inlet heights (H_{col}): 2 m, 2.5 m and 3 m. A moderate reduction in power can clearly be seen at these three heights, as shown in Figure 16(a). The bar indicating 2 m shows the maximum power, above 49 kW. Thereafter, the power experiences a slight decrease at 2.5 m, before stabilizing at 3 m, where it remains close to 47.8 kW. Between 2 m and 3 m, the power recorded a decrease of 3.1 %.

These variations, although minimal, suggest a possible influence of the collector height on the generated power, although this influence is not drastic in the studied range. However, regarding the mass flow rate (Figure 16(b)), at first glance, a relatively constant mass flow rate of around 1300 kg/s is observed for these three heights. However, a closer observation reveals slight variations. The collector height exerts a limited influence in the range of 2 to 3 m, with a slight decrease in mass flow rate of 4.2 kg/s observed between 2 m and 3 m. This is explained by the fact that a greater collector height reduces the air inlet velocity into the chimney due to a decrease in the pressure gradient, which decreases the mass flow rate and, consequently, the power generated.

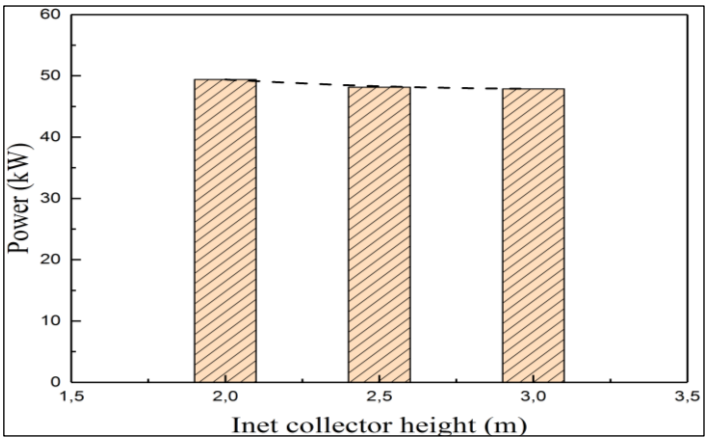

(a)

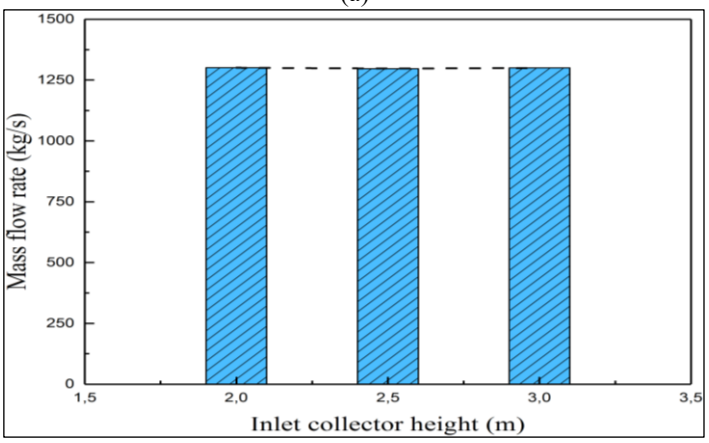

(b)

Figure 16. Inlet collector height effect on: (a) output power plant and (b) mass flow rate
Source: Authors, (2025).

According to Figure 17, the air temperature does not change along the collector because the amount of heat transferred to the air remains proportional to the mass flow rate. If the flow rate decreases (due to reduced velocity), the residence time of the air in the collector increases, compensating for the decrease in the convective heat transfer coefficient (Figure 17(b)). Thus, the heat absorbed per unit mass of air remains the same, maintained by a balance between residence time and heat transfer efficiency. Increasing the inlet height expands the initial cross-sectional area of the collector. According to the continuity equation, for a constant mass flow rate, an increase in the collector inlet area leads to a decrease in the inlet velocity (Figure 171(a)). However, further down the collector, the geometry stabilizes (constant cross-sectional area or balance between buoyancy and pressure drops), which maintains a constant velocity despite the initial reduction.

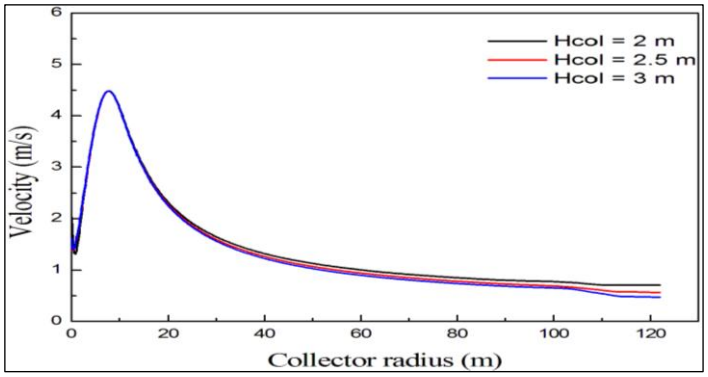

(a)

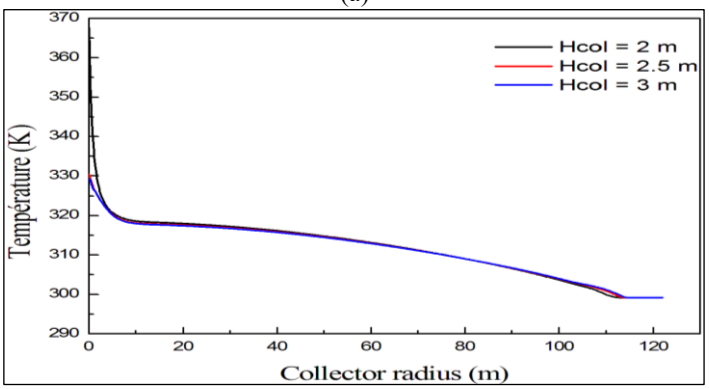

(b)

Figure 17: Inlet collector height effect on: (a) velocity and (b) temperature.
Source: Authors, (2025).

V.8 OUPUT POWER OPTIMIZATION

Figure 18 shows the evolution of the power and efficiency generated by the solar chimney as a function of its dimensions, under identical conditions for all tests. The quantitative analysis reveals a significant heterogeneity in the influence of these parameters, as illustrated in detail by Table 4.

Table 4: The percentage increase in SCPP performance (%).

Parameter	Rate of increase (%)			
H_{col} (m)	+25, +50			
H (m)		+25, +50		
R (m)			+40, +100	
Angle divergence (°)				+0.57, +1.43
Power (kW)	-2.53, -3.1	+26.3, +52.3	+6.67, +22.89	+0.21, +3.18

Source: Authors, (2025).

This result mainly highlights, firstly, the considerable effect of the chimney height. For example, if the height of the chimney, which generates a power of 49.4 kW at 200 m in the reference case, were increased to 300 m, the output power would increase by about 52.3 %, reaching almost 75.24 kW, with an efficiency of 43.57 %.

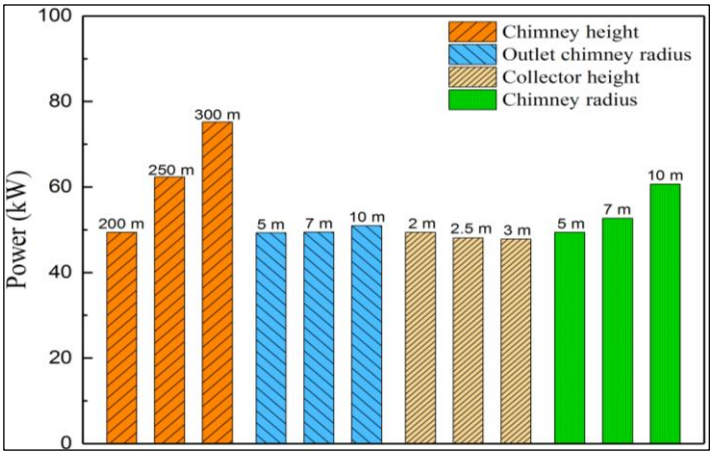

(a)

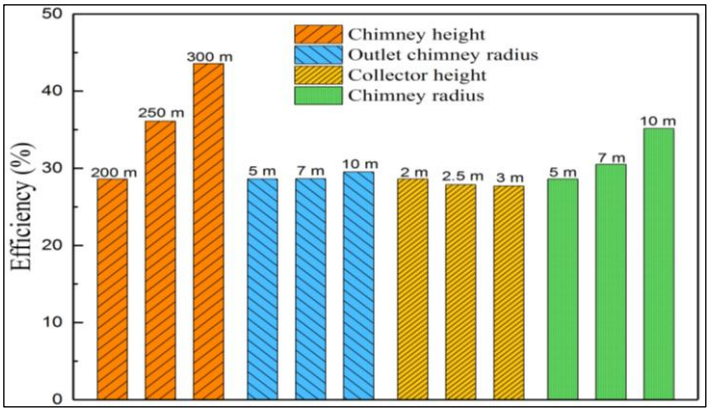

(b)

Figure 18: Variation under various parameters of: (a) output power plant and (b) chimney efficiency.
Source: Authors, (2025).

VI. CONCLUSIONS

The study of solar chimney performance was approached through an analysis of the effect of various geometric parameters and the adoption of different turbulence models, all supported by numerical simulations via CFD. These investigations highlighted the crucial importance of modeling for the accurate prediction of the behavior of these systems. The evaluation of the ability of turbulence models to simulate the flow in a solar chimney reveals significant disparities and underlines the importance of careful turbulence model selection. It is essential to conduct a thorough examination to identify the most appropriate turbulence model that aligns with the unique geometry and operational conditions. Simply selecting a turbulence model at random may not adequately capture the subtleties of the flow in the solar chimney. This could potentially lead to misleading results that do not accurately represent the physical reality, or worse, produce erroneous results that compromise the efficiency and reliability of the solar chimney. In this study, among the evaluated models, the RNG k-ε turbulence model stood out for its best agreement with the experimental data available in the literature, validating its ability to faithfully capture the essential physical phenomena.

On the other hand, through an analysis of the effect of various geometric parameters, the performance of a solar chimney, in terms of power, mass flow rate or air velocity and temperature, is strongly influenced by its dimensions. The performance of a solar chimney depends on a subtle balance between thermodynamic expansion and flow stability. A large uniform radius favors mass flow rate by stabilizing the flow, while a marked divergence angle locally optimizes velocity and temperature reduction to the detriment of the overall flow rate. The increased height at the collector inlet locally reduces the velocity by increasing the surface area, while the temperature remains stable thanks to a dynamic thermal balance. Furthermore, a greater height generates a higher mass flow rate and significantly amplifies the generated power. To obtain maximum power, it is essential to use a chimney that is both tall and wide, as well as a low collector, which optimizes thermal draft and reduces heat loss. The mass flow rate is mainly determined by the diameter of the chimney, a larger diameter facilitating the air flow. The chimney height has a significant and proportional impact on the output power, while the collector height has a minimal effect, inversely proportional to the power generated in the considered ranges.

VII. AUTHOR'S CONTRIBUTION

Conceptualization: Farid Gaci.
Methodology: Farid Gaci, Ahcene Akni, Moumtez Bensouici.
Investigation: Farid Gaci, Mohamed walid Azizi, Ahcene Akni, Moumtez Bensouici, Djoubeir Debbah.
Discussion of results: Farid Gaci, Ahcene Akni, Moumtez Bensouici.
Writing – Original Draft: Farid Gaci.
Writing – Review and Editing: Farid Gaci, Mohamed walid Azizi, Ahcene Akni, Moumtez Bensouici.
Resources: Farid Gaci, Mohamed walid Azizi, Ahcene Akni, Moumtez Bensouici, Djoubeir Debbah.
Supervision: Mohamed walid Azizi, Ahcene Akni, Moumtez Bensouici.
Approval of the final text: Farid Gaci, Mohamed walid Azizi, Ahcene Akni, Moumtez Bensouici, Djoubeir Debbah.

VIII. ACKNOWLEDGMENTS

The authors would like to extend their heartfelt thanks to the Directorate General of Scientific Research and Technological Development (DGSRTD) for their assistance in this project.

IX REFERENCES

[1] J. Schlaich, The Solar Chimney: Electricity from the Sun. Stuttgart, Germany: Axel Menges, 1995.

[2] N. Pasumarthi and S. A. Sherif, "Experimental and theoretical performance of a demonstration solar chimney model—Part I: Mathematical model development," Int. J. Energy Res., vol. 22, no. 3, pp. 277–288, 1998.

[3] P. Das and V. P. Chandramohan, "Experimental studies of a laboratory scale inclined collector solar updraft tower plant with thermal energy storage system," J. Build. Eng., vol. 41, p. 102394, 2021.

[4] P. Das and V. P. Chandramohan, “Performance characteristics of divergent chimney solar updraft tower plant,” Int. J. Energy Res., pp. 1–16, 2020.

[5] K. Ahmed, S. Algburi, Z. H. Ali, A. K. Ahmed, and H. N. Shubat, “Hybrid solar chimneys: A comprehensive review,” Energy Rep., vol. 8, pp. 438–460, 2022.

[6] H. Nasraoui, Z. Driss, and H. Kchaou, “Novel collector design for enhancing the performance of solar chimney power plant,” Renew. Energy, vol. 145, pp. 1658–1671, 2020.

[7] F. Murena, I. Gaggiano, and B. Mele, “Fluid dynamic performances of a solar chimney plant: Analysis of experimental data and CFD modelling,” Energy, vol. 249, p. 123702, 2022.

[8] R. K. Kumar, N. V. V. K. Chaitanya, and N. S. Kumar, “Solar thermal energy technologies and its applications for process heating and power generation – A review,” J. Clean. Prod., vol. 282, 2021.

[9] A. Ayadi, A. Bouabidi, Z. Driss, and M. S. Abid, “Experimental and numerical analysis of the collector roof height effect on the solar chimney performance,” Renew. Energy, vol. 115, pp. 649–662, 2018.

[10] Y. Wu, T. Ming, R. de Richter, R. Höffer, and H. J. Niemann, “Large-scale freshwater generation from the humid air using the modified solar chimney,” Renew. Energy, vol. 146, pp. 1325–1336, 2020.

[11] S. H. Fallah and M. S. Valipour, “Evaluation of solar chimney power plant performance: the effect of artificial roughness of collector,” Sol. Energy, vol. 188, pp. 175–184, 2019.

[12] H. Kebabsa, M. S. Lounici, M. Lebbi, and A. Daimallah, “Thermo-hydrodynamic behavior of an innovative solar chimney,” Renew. Energy, vol. 145, pp. 2074–2090, 2020.

[13] P. Guo, J. Li, and Y. Wang, “Numerical simulations of solar chimney power plant with radiation model,” Renew. Energy, vol. 62, pp. 24–30, 2014.

[14] A. Mebarki et al., “CFD analysis of solar chimney power plant: Finding a relationship between model minimization and its performance for use in urban areas,” Energy Rep., vol. 8, pp. 500–513, 2022.

[15] A. Hassan, M. Ali, and A. Waqas, “Numerical investigation on performance of solar chimney power plant by varying collector slope and chimney diverging angle,” Energy, vol. 142, pp. 411–425, 2018.

[16] C. B. Maia, A. G. Ferreira, R. M. Valle, and M. F. B. Cortez, “Theoretical evaluation of the influence of geometric parameters and materials on the behavior of the air flow in a solar chimney,” Comput. Fluids, vol. 38, pp. 625–636, 2009.

[17] H. A. E. Mohamad, M. Elsamadony, and M. Ramon, “A Computational Fluid Dynamics Study on Different Solar Chimney Designs on Solar Radiation,” J. Eng. Res., vol. 5, no. 1, pp. 31–37, 2021.

[18] A. B. Awan, V. V. Kotturu, C. Mouli, and M. Zubair, “Performance enhancement of solar tower power plant: A multi-objective optimization approach,” Energy Convers. Manag., vol. 225, p. 113378, 2020.

[19] M. R. Torabi et al., “Investigation the performance of solar chimney power plant for improving the efficiency and increasing the outlet power of turbines using computational fluid dynamics,” Energy Rep., vol. 7, pp. 4555–4565, 2021.

[20] M. Jirena, R. Bhoraniya, and A. Harichandan, “CFD analysis of solar chimney power plant: effect of chimney height, shape and collector size,” J. Sol. Energy Res., vol. 4, no. 1, pp. 61–71, 2019.

[21] Y. Noorollahi et al., “Reliable renewable power production by modeling of geothermal assisted solar chimney power plant,” Geothermics, vol. 111, p. 102701, 2023.

[22] E. Gholamalizadeh and M. H. Kim, “CFD analysis of a solar chimney power plant with inclined collector roof,” Energy, vol. 107, pp. 661–667, 2016.

[23] S. Montelpare, V. D’Alessandro, A. Zoppi, and E. Costanzo, “A solar chimney for renewable energy production: thermo-fluid dynamic optimization by CFD analyses,” IOP Conf. Ser.: J. Phys.: Conf. Ser., vol. 923, no. 1, p. 012047, 2017.

[24] L. Zuo et al., “Performance analysis of a wind supercharging solar chimney power plant combined with thermal plant for power and freshwater generation,” Energy Convers. Manag., vol. 204, p. 112282, 2020.

[25] C. B. Maia, A. G. Ferreira, L. Cabezas-Gomez, J. de Oliveira Castro Silva, and S. de Morais Hanriot, “Thermodynamic analysis of the drying process of bananas in a small-scale solar updraft tower in Brazil,” Renew. Energy, vol. 114, pp. 1005–1012, 2017.

[26] F. F. Daghistani, “Solar chimney street-lighting pole for ventilating polluted urban areas,” Sustain. Cities Soc., vol. 72, p. 103057, 2021.

[27] H. Xiong et al., “Numerical analysis of a negative emission technology of methane to mitigate climate change,” Sol. Energy, vol. 255, pp. 416–424, 2023.

[28] A. A. Serageldin, A. K. Abdelrahman, and S. Ookawara, “Parametric study and optimization of a solar chimney passive ventilation system coupled with an earth-to-air heat exchanger,” Sustain. Energy Technol. Assess., vol. 30, pp. 263–278, 2018.

[29] A. Sellami, D. Benlahcene, A. H. Benmachiche, and Z. Aouachria, “Performance analysis of a solar chimney power plant system in two Algeria regions,” Int. J. Ambient Energy, pp. 1–12, 2021.